

## RESEARCH ARTICLE

## Role of Compressibility on Tsunami Propagation

10.1002/2017JC013054

Ali Abdolali<sup>1,2</sup>  and James T. Kirby<sup>3</sup> 

## Key Points:

- The role of ocean compressibility on tsunami propagation is discussed
- A Mild Slope Equation for Weakly Compressible fluid is derived, validated, and tested for simplified and realistic cases
- The model equation is used to reconstruct Tohoku-oki 2011 tsunami event and compared to in situ measurements

## Correspondence to:

A. Abdolali,  
ali.abdolali@noaa.gov

## Citation:

Abdolali, A., & Kirby, J. T. (2017). Role of compressibility on tsunami propagation. *Journal of Geophysical Research: Oceans*, 122. <https://doi.org/10.1002/2017JC013054>

Received 3 MAY 2017

Accepted 27 NOV 2017

Accepted article online 30 NOV 2017

<sup>1</sup>NWS/NCEP/Environmental Modeling Center, National Oceanic and Atmospheric Administration, College Park, MD, USA, <sup>2</sup>University Corporation for Atmospheric Research, Boulder, CO, USA, <sup>3</sup>Center for Applied Coastal Research, Department of Civil and Environmental Engineering, University of Delaware, Newark, DE, USA

**Abstract** In the present paper, we aim to reduce the discrepancies between tsunami arrival times evaluated from tsunami models and real measurements considering the role of ocean compressibility. We perform qualitative studies to reveal the phase speed reduction rate via a modified version of the Mild Slope Equation for Weakly Compressible fluid (MSEWC) proposed by Sammarco et al. (2013). The model is validated against a 3-D computational model. Physical properties of surface gravity waves are studied and compared with those for waves evaluated from an incompressible flow solver over realistic geometry for 2011 Tohoku-oki event, revealing reduction in phase speed.

**Plain Language Summary** Submarine earthquakes and submarine mass failures (SMFs), can generate long gravitational waves (or tsunamis) that propagate at the free surface. Tsunami waves can travel long distances and are known for their dramatic effects on coastal areas. Nowadays, numerical models are used to reconstruct the tsunamigenic events for many scientific and socioeconomic aspects i.e. Tsunami Early Warning Systems, inundation mapping, risk and hazard analysis, etc. A number of typically neglected parameters in these models cause discrepancies between model outputs and observations. Most of the tsunami models predict tsunami arrival times at distant stations slightly early in comparison to observations. In this study, we show how ocean compressibility would affect the tsunami wave propagation speed. In this framework, an efficient two-dimensional model equation for the weakly compressible ocean has been developed, validated and tested for simplified and real cases against three dimensional and incompressible solvers. Taking the effect of compressibility, the phase speed of surface gravity waves is reduced compared to that of an incompressible fluid. Then, we used the model for the case of devastating Tohoku-Oki 2011 tsunami event, improving the model accuracy. This study sheds light for future model development to include ocean compressibility among other typically neglected parameters.

## 1. Introduction

Most existing tsunami propagation models consider the ocean to be an incompressible, homogenous medium. Recently, it has become clear that models of this type predict tsunami arrival times at distant stations which are slightly early in comparison to observations. Part of this discrepancy may be attributed to the neglect of frequency dispersion in a number of operational models, which slow the waves relative to the prediction of shallow water theory, but corrections afforded by this effect in Boussinesq or nonhydrostatic models (Baba et al., 2015; Kirby et al., 2013; Yamazaki et al., 2011) only account for a portion of the observed discrepancy. See for example, the discussion of arrival of waves from the Tohoku-oki event at DART buoy #32411 offshore of Panama in Kirby et al. (2013). A number of studies have attributed the observed delay of arrival to additional physical features including thermal or salinity-based density stratification (Allgeyer & Cummins, 2014; Watada, 2013), compressibility of the water column (Allgeyer & Cummins, 2014; Dalrymple & Rogers, 2007; Wang, 2015; Watada, 2013), and elastic deformation of the underlying solid earth (Allgeyer & Cummins, 2014; Eyov et al., 2013; Watada et al., 2014). Taking a number of typically neglected effects together, the phase speed of surface gravity waves is reduced compared to that of an incompressible fluid due to the combined effects of compressibility, stratification, and elasticity (Baba et al., 2017). Wang (2015) introduced a depth correction in a shallow water model in order to mimic the effects of compressibility without changing the governing equations. The long period dispersion effect due to

seawater compressibility, density stratification, bottom elasticity, and gravitational potential changes can rival the size of the short period dispersions embedded in Boussinesq equation. Boussinesq models consider the effects of frequency dispersion especially in intermediate and shallow waters, which are increasingly coming into use as ocean basin scale tsunami propagation models. The capabilities of these models have been expanded considering the effects of earth rotation and Coriolis forces on propagation of tsunami waves in global scale. Taking into account the aforementioned parameters can improve the accuracy of model descriptions of basin scale wave propagation (Kirby et al., 2013; Løvholt et al., 2008; Yamazaki et al., 2011).

In the last decade, studies have shown the advantages to be gained by taking the compressibility of water into account in describing the behavior of the water column in a tsunami source region (Levin & Nosov, 2016). Also, hydroacoustic waves generated by tsunamigenic sources due to the compressibility of water column gain attentions by many researchers as tsunami precursor as a component of Tsunami Early Warning Systems (Abdolali et al., 2015a; Cecioni et al., 2015; Stiassnie, 2010).

Here a simplified example showing the effect of compressibility in tsunami wave propagation speed is performed using two 3-D solvers in constant depth for the compressible and incompressible fluids. The model equations are described in section 2. We use  $h = 4,000$  m,  $c = 1,500$  m/s, and  $\rho = 1,000$  kg/m<sup>3</sup>. The other parameters are for a unit sudden elevation of source area with semilength  $b = 30$  km and rise time  $\tau = 10$  s. The results are depicted in Figure 1, which show the time series of free-surface  $\eta$  at 1,000 km from the epicenter. The black line shows the time series of free-surface elevation from incompressible water model while the blue line shows the results from a compressible model. The time lag,  $\Delta t$ , between the arrival of surface gravity waves obtained from these models are highlighted in the figure.

Three-dimensional (3-D) numerical models for simulation of surface gravity and hydroacoustic waves over large-scale geometries within the framework of compressible fluids are computationally expensive. Nosov and Kolesov (2007) have used a three-dimensional numerical model to study the Tokachi-oki 2003 tsunami event on a regional domain. A practical solution for large-scale applications would be depth-integrated numerical models. Sammarco et al. (2013) have proposed a hyperbolic Mild Slope Equation for Weakly Compressible fluid, MSEWC, over rigid bottom. Subsequently, Abdolali et al. (2015b) derived the hyperbolic Mild Slope Equation for Dissipative Weakly Compressible fluids, MSEDWC, accounting for damping induced by viscoelastic properties of a deformable bottom.

In this paper, we modify the mild-slope formulation of Sammarco et al. (2013) to include the effects of ocean compressibility in order to reduce the discrepancy between propagation speed of surface gravity waves given from in situ measurement and model simulation. Governing equations and the resulting eigenvalues, eigenfunctions and dispersion relation for monochromatic wave components are presented in section 2. In section 3, we derive a modified MSEWC which extends the original formulation of Sammarco et al.

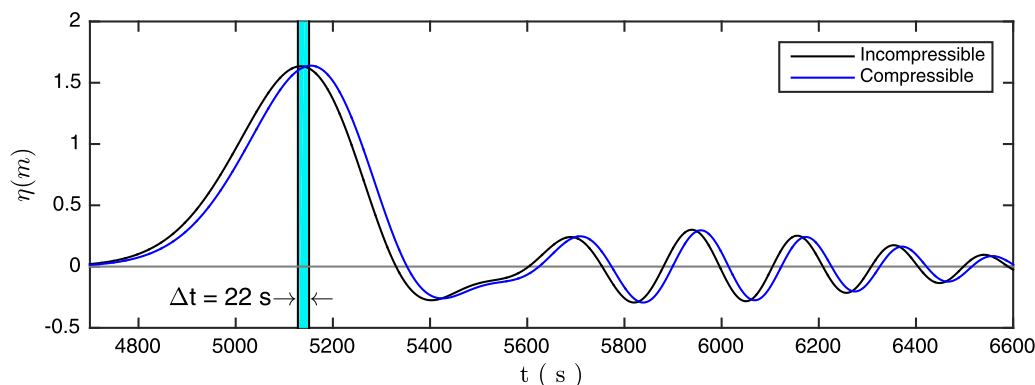


**Figure 1.** Time lag in tsunami arrival time in term of free-surface records at a distance of  $x = 1,000$  km from the epicenter. Results of a sample computation carried out using two 3-D flow solvers in a constant depth,  $h = 4,000$  m, for a unit source area with semilength  $b = 30$  km and rise time  $\tau = 10$  s, evaluated by the incompressible solver (black line) and the compressible solver (3) (blue line). The peak arrival times are shown by vertical lines correspond to wave speed calculated from (equation (14)).

(2013) to account for the compressibility of the static ocean. Verification of the mild-slope equation model is carried out for constant and varying geometries against a fully 3-D model in section 4. In section 5, following Tappin et al. (2014) and Abdolali et al. (2017), the generation mechanism of the 2011 Tohoku-oki is modeled as a combination of the space and time varying coseismic seafloor deformation caused by the earthquake followed by a submarine mass failure (SMF) to justify the mismatch between arrival time at far field gauges, calculated from incompressible models. Conclusions are given in section 6.

## 2. Governing Equations

Consider a three-dimensional Cartesian coordinate system  $\mathbf{x}=(x, y, z)$  with the origin in the undisturbed free surface, and the  $z$  axis oriented vertically upward. The governing equations for inviscid motion of a compressible medium are given by

$$\begin{aligned} \rho_t + \nabla \cdot (\rho \mathbf{u}) &= 0 \\ \mathbf{u}_t + (\mathbf{u} \cdot \nabla) \mathbf{u} + \frac{1}{\rho} \nabla p &= -g \mathbf{i}_z \end{aligned} \quad (1)$$

where  $g$  is gravitational acceleration,  $\rho$  is fluid density,  $p$  is pressure, and  $\mathbf{u}$  is velocity. Equations (1) require an additional closure relating density to pressure,  $\rho = \rho(p)$ . We express this in terms of density and pressure variations as  $d\rho = (d\rho/dp)dp = dp/c^2$ , where  $c$  is sound speed in water and is taken to be constant. With viscosity neglected and the assumed relation between density and pressure, the conditions for the existence of a velocity potential are satisfied, and we write  $\mathbf{u} = \nabla \Phi$ . A basic, hydrostatic ocean state may then be defined as

$$\rho_0(z) = \rho_s e^{-\gamma z}; \quad p_0(z) = \frac{\rho_s g}{\gamma} (e^{-\gamma z} - 1); \quad \mathbf{u} = 0 \quad (2)$$

where  $\gamma = g/c^2$  is the lapse rate for density and pressure with elevation. After linearizing about the basic state, the equation governing  $\Phi$  is given by (Bondi, 1947)

$$\Phi_{tt} - c^2 (\nabla_h^2 \Phi + \Phi_{zz}) = -g \Phi_z; \quad -h \leq z \leq 0 \quad (3)$$

where  $\nabla_h$  is the horizontal gradient operator and subscripts on dependent variables denote partial derivatives. Equation (3) follows from the use of the complete expressions (2) for background density and pressure; however, in practice these are well approximated by the leading order expressions retaining compressibility effects:

$$\rho_0(z) = \rho_s (1 - \gamma z); \quad p_0(z) = -\rho_s g z \left( 1 - \frac{1}{2} \gamma z \right) \quad (4)$$

The linearized boundary conditions at the free surface,  $z = 0$ , and the impermeable (but possibly moving) bottom,  $z = -h$ , are

$$\begin{aligned} g \Phi_z + \Phi_{tt} &= 0; & z = 0 \\ \Phi_z + h_t + \nabla_h \Phi \cdot \nabla_h h &= 0; & z = -h \end{aligned} \quad (5)$$

For the case of a flat bottom, the velocity potential for a given angular frequency  $\omega$  may be expanded in terms of plane waves:

$$\Phi(x, y, z, t) = \sum_{n=0}^{\infty} f_n(z) e^{i(k_n x - \omega t)} \quad (6)$$

where  $k_n$  are the modal wave numbers. Substituting (6) in (3)–(5) with  $h$  constant gives the boundary value problem (BVP):

$$\begin{aligned} f_n'' - \gamma f_n' - \beta_n^2 f_n &= 0 \\ f_n'(-h) &= 0 \\ g f_n'(0) - \omega^2 f_n(0) &= 0 \end{aligned} \quad (7)$$

where  $\beta_n^2 = k_n^2 - \omega^2/c^2$  is the separation constant for the case of density/pressure fluctuations in an otherwise constant density ocean (Sammarco et al., 2013). The problem is put in Sturm-Liouville form by the substitution:

$$f_n(z) = \tilde{f}_n(z) e^{\gamma z/2} \quad (8)$$

yielding the eigenvalue problem:

$$\begin{aligned} \tilde{f}_n'' - \tilde{\beta}_n^2 \tilde{f}_n &= 0 \\ \tilde{f}_n'(-h) + \frac{\gamma}{2} \tilde{f}_n(-h) &= 0 \\ \tilde{f}_n'(0) + \left( \frac{\gamma}{2} - \frac{\omega^2}{g} \right) \tilde{f}_n(0) &= 0 \end{aligned} \quad (9)$$

with  $\tilde{\beta}_n^2 = \beta_n^2 + (\gamma/2)^2$ . The problem yields eigenfunctions  $\tilde{f}_n(z)$ , normalized to a value of unity at  $z = 0$ , given by

$$\tilde{f}_n(z) = \frac{\cosh(\tilde{\beta}_n(h+z)) - (\gamma/(2\tilde{\beta}_n)) \sinh(\tilde{\beta}_n(h+z))}{\cosh(\tilde{\beta}_n h) - (\gamma/(2\tilde{\beta}_n)) \sinh(\tilde{\beta}_n h)} \quad (10)$$

The dispersion relation governing  $\tilde{\beta}_n$  is given by (11) (Dalrymple & Rogers, 2007; Kadri, 2015; Kadri & Stiassnie, 2013):

$$\omega^2 \left[ 1 - (\gamma/(2\tilde{\beta}_n)) \tanh \tilde{\beta}_n h \right] = g \tilde{\beta}_n (1 - (\gamma/(2\tilde{\beta}_n))^2) \tanh \tilde{\beta}_n h \quad (11)$$

The real root  $\tilde{\beta}_0$  of the dispersion relation (11) represents the primary surface gravity wave modified by compressibility effects, while the imaginary roots  $\tilde{\beta}_n$ ,  $n \geq 1$  describe both progressive and spatially decaying hydroacoustic modes, which are generated within compressible flow framework together with surface gravity waves. For the case of gravity and hydroacoustic waves propagating in a constant density ocean without static compressibility, the dispersion relation and eigenfunctions reduce to the forms:

$$\omega^2 = g \beta_n \tanh(\beta_n h) \quad (12)$$

$$f_n(z) = \frac{\cosh(\beta_n(h+z))}{\cosh(\beta_n h)} \quad (13)$$

as in Sammarco et al. (2013).

The solution of the dispersion relation (11) is depicted in Figure 2 for surface gravity wave ( $n = 0$ ) and in Figure 3 for acoustic modes ( $n \geq 1$ ), in the range of 0.1–10 km water depth. In Figure 2, the phase speed calculated for compressible ocean with constant density (dashed line) and for variable density (solid line) are shown for frequencies in the range of 0.0001–0.1 Hz and for 1–6 km water depth. Note that for realistic, variable depth bathymetries near subductions zones, tsunami waves propagate over large depth ( $\sim 5$ –6 km) for short

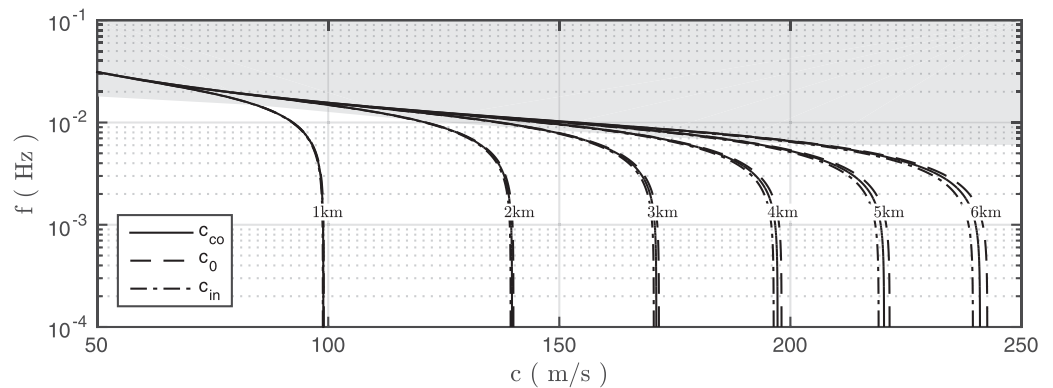


**Figure 2.** Phase speed for varying water depth (1 km increments) for a compressible (solid lines) and incompressible ocean (dashed lines). For incompressible ocean, the wave number is given by  $k_n = \beta_n$  where  $\beta_n$  is the solution of dispersion relation (equation (12)). For compressible ocean with constant density, the wave number is given by  $k_n^2 = \beta_n^2 + \omega^2/c^2$  where  $\beta_n$  is the solution of dispersion relation (equation (12)). For compressible ocean with variable density, the wave number is given by  $k_n^2 = \tilde{\beta}_n^2 - \gamma^2/4 + \omega^2/c^2$  where  $\tilde{\beta}_n$  is the solution of dispersion relation (equation (11)). The shaded area represents the frequency range corresponding to short waves ( $\lambda \leq 5h$ ), where  $\lambda$  is wavelength.

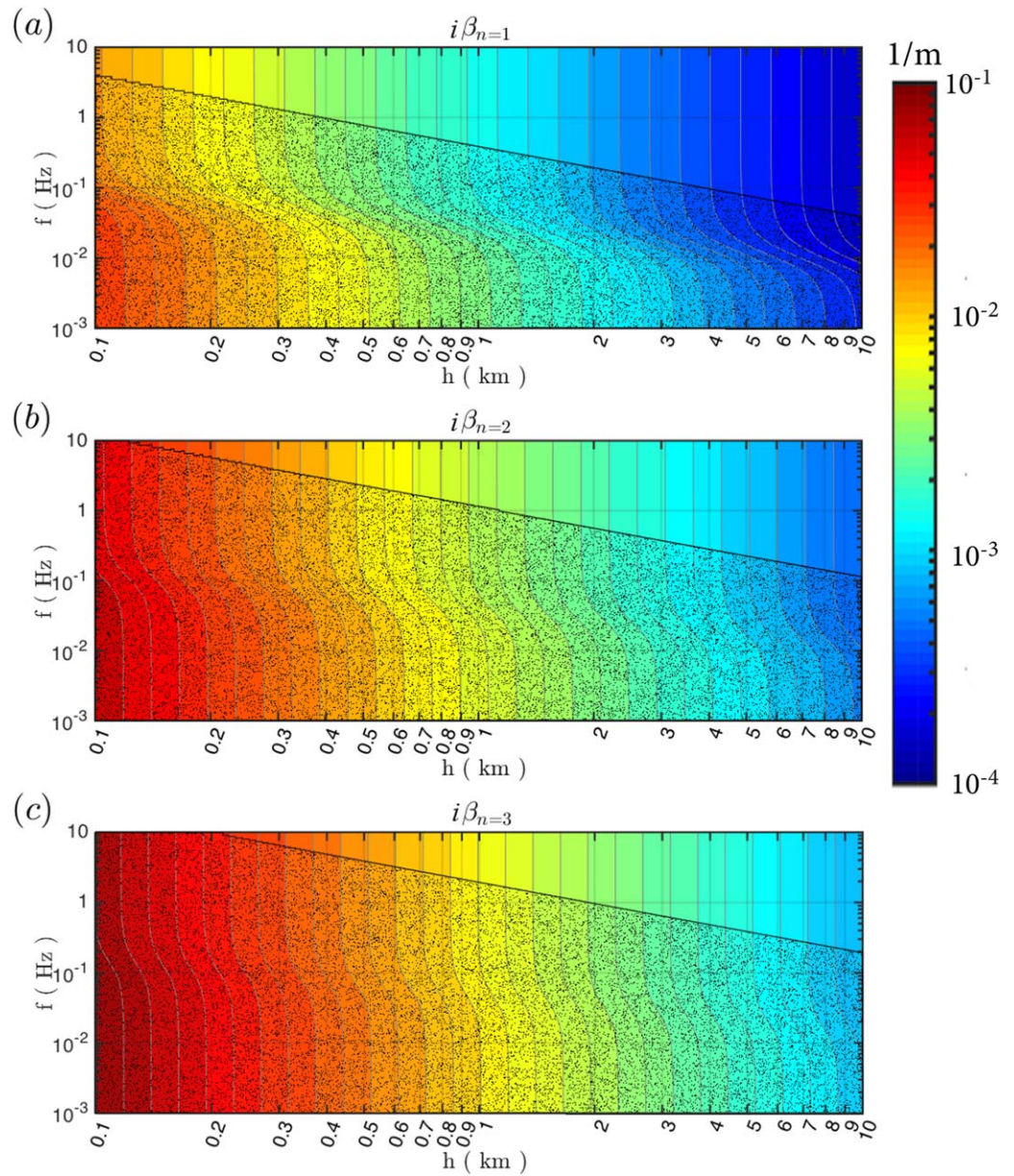


**Figure 3.** Imaginary roots of dispersion relation  $\beta_n$  for varying water depth (0.1–10 km),  $n$ th modes are shown in a–c. The wave number is given from solution of dispersion relation (11). The evanescent modes are shown by shaded areas in each subplot where  $k_n^2 = \omega^2/c^2 + \beta_n^2 \leq 0$ .

distances and usually propagate over  $h \leq 4$  km depth. In the shallow water limit,  $kh \ll 1$ , the classical phase speed  $c_0$  for incompressible motion, the phase speed  $c_{in}$  evaluated for compression waves in a constant density medium (12) and  $c_{co}$  evaluated from (11) for waves in a compressed, variable density medium, are given by

$$\begin{aligned}
 c_0 &= \sqrt{gh} \\
 c_{in} &= c_0 \left( 1 - \frac{1}{2} \gamma h \right) = c_0 \left( 1 - \frac{1}{2} M^2 \right) \quad kh \ll 1 \\
 c_{co} &= c_0 \left( 1 - \frac{1}{4} \gamma h \right) = c_0 \left( 1 - \frac{1}{4} M^2 \right)
 \end{aligned} \tag{14}$$

where  $M = \sqrt{gh}/c = c_0/c$  is a Mach number based on the linear incompressible surface longwave speed. Note that neglect of the static compressibility of the ocean itself in models for hydroacoustic fluctuations

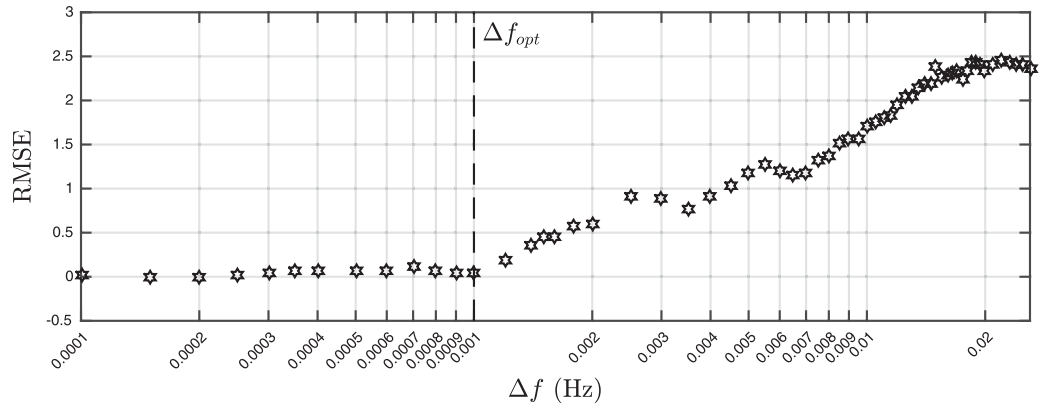


**Figure 4.** Frequency band optimization of source spectrum. The vertical dashed line shows the maximum allowable value  $\Delta f_{opt}$  in 2-D model, which successfully reconstructs 3-D wave train.

leads to an overestimation of the phase speed reduction relative to the incompressible case. As it is shown by shaded area in Figure 1, the time lag between compressible and incompressible model results at the distance of  $x = 1,000$  km can be evaluated by  $\Delta t = x/c_{co} - x/c_0 = 22$  s.

In Figure 3, the first three imaginary separation constants, representing acoustic modes, are shown in each subplot. The shaded area in each subplot shows the range for evanescent modes where  $k_n^2 = \omega^2/c^2 + \beta_n^2 \leq 0$ .

### 3. Mild-Slope Equation

We develop a mild-slope equation based on the eigenfunction structure for the problem with constant layer depth  $h$ . We use the governing equation and boundary conditions described in section 2 to derive the mild-slope model using an approach described in Sammarco et al. (2013) and Abdolali et al. (2015b). The hypothesis of a mild slope allows us to seek a solution in the form:

$$\Phi(x, y, z, t) = \sum_{n=0}^{\infty} \tilde{f}_n(x, y, z) e^{\frac{z}{2}} \tilde{\phi}_n(x, y, t) \tag{15}$$

Reformulating the governing equation (3) equivalently in terms of the  $\tilde{f}_n$  and  $\tilde{\phi}_n$  and substituting  $g = c^2 \gamma$  and first and second derivatives of (8), we obtain

$$\sum_{n=0}^{\infty} \left[ \frac{1}{c^2} (\tilde{f}_n \tilde{\phi}_n)_{tt} - \nabla_h^2 (\tilde{f}_n \tilde{\phi}_n) - \tilde{f}_{nzz} \tilde{\phi}_n + \left(\frac{\gamma}{2}\right)^2 \tilde{f}_n \tilde{\phi}_n \right] = 0 \tag{16}$$

where  $\tilde{f}_{nz}$  and  $\tilde{f}_{nzz}$  are

$$\tilde{f}_{nz} = \left( \tilde{f}_{nz} + \frac{\gamma}{2} \tilde{f}_n \right) e^{\frac{z}{2}} \tag{17}$$

$$\tilde{f}_{nzz} = \left[ \tilde{f}_{nzz} + 2 \left(\frac{\gamma}{2}\right) \tilde{f}_{nz} + \left(\frac{\gamma}{2}\right)^2 \tilde{f}_n \right] e^{\frac{z}{2}} \tag{18}$$

Multiplying (16) by  $\tilde{f}_m$ , integrating over the depth, invoking the orthogonality of the  $\tilde{f}_n$ 's and using Leibnitz' rule and boundary conditions (5) finally gives

$$\left[ \left( \frac{l_1^n}{c^2} + \frac{1}{g} \right) \tilde{\phi}_{n,t} \right]_{,t} - \nabla_h \cdot \left( l_1^n \nabla_h \tilde{\phi}_n \right) + \left[ l_2^n + \left(\frac{\gamma}{2}\right)^2 l_1^n \right] \tilde{\phi}_n + \frac{\gamma}{2} \left[ 1 - \tilde{f}_n^2(-h) \right] \tilde{\phi}_n = \tilde{f}_n(-h) e^{-\gamma z/2} h_t \tag{19}$$

where we have neglected products of first-order spatial and temporal derivatives of the vertical eigenfunctions  $\tilde{f}_n$ . The model coefficients are given by

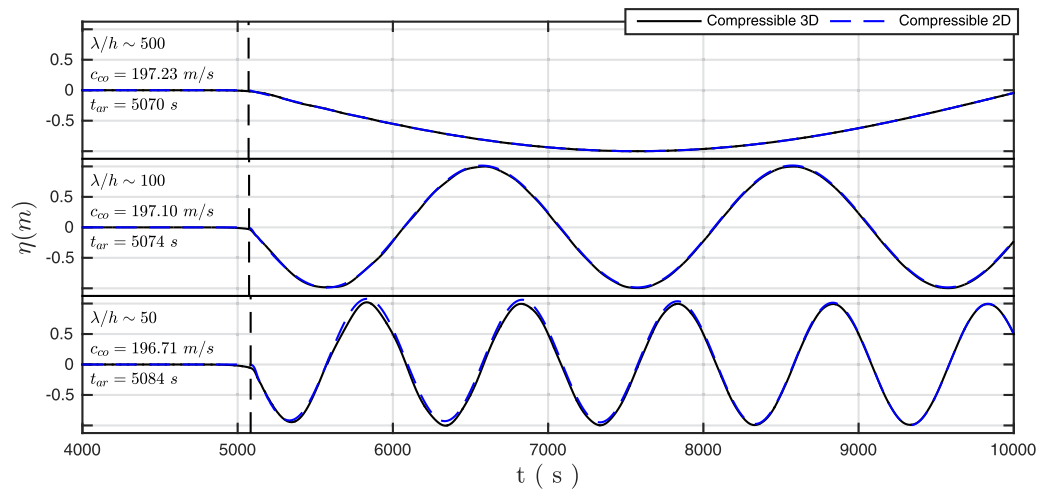


**Figure 5.** Results for the free-surface elevation time series,  $\eta$ , at  $x = 1,000$  km from the monochromatic wave generator according to the 3-D (solid line) and depth-integrated (dashed line) models in a constant depth ( $h = 4$  km). The dimensionless wavelength ( $\lambda/h$ ), phase celerity ( $c_{co}$ ), and signal arrival time ( $t_{ar}$ ) (vertical dashed line) correspond to three monochromatic wave frequencies, (top)  $f = 0.0001$  Hz, (middle)  $f = 0.0005$  Hz, and (bottom)  $f = 0.001$  Hz, are calculated from the solution of dispersion relation presented in equation (14).

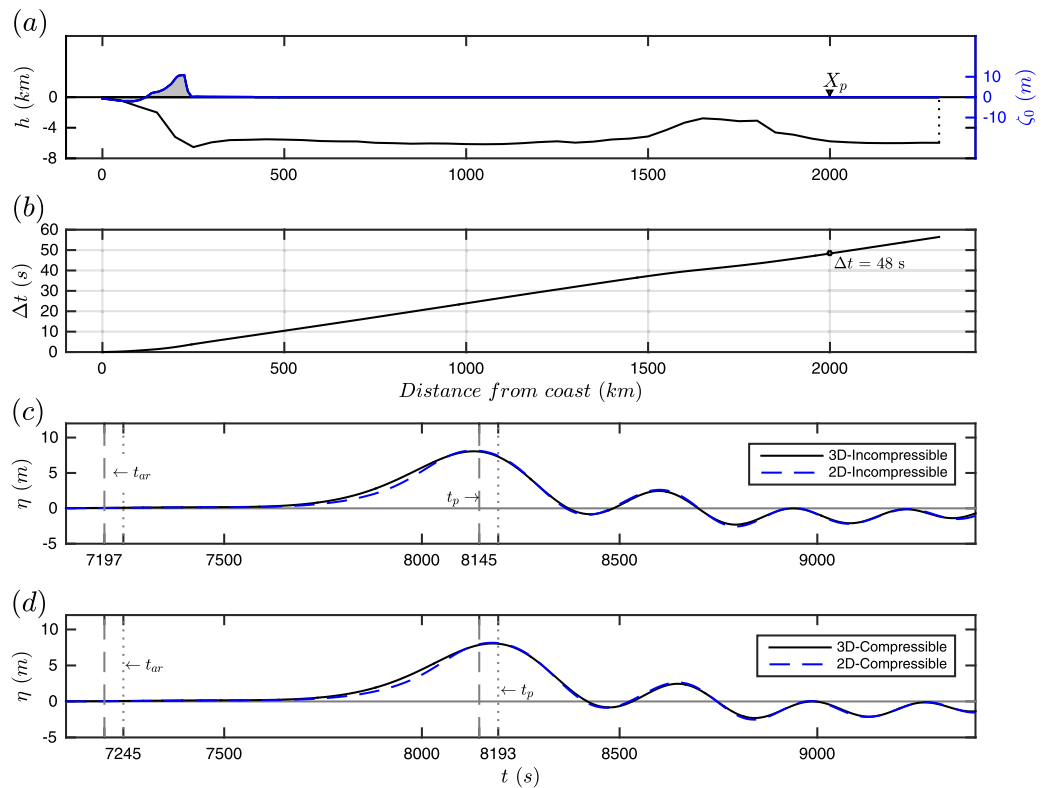


**Figure 6.** (a) Residual seabed displacement ( $\zeta_0$ ) and water depth ( $h$ ) for the vertical section A shown in Figure 7, which crosses the 2011 Tohoku-oki earthquake; (b) the difference between arrival time,  $\Delta t$ , calculated from incompressible and compressible models. Time series of free surface ( $\eta$ ) at  $X_p = 2,000$  km calculated by the solution of (c) the incompressible solvers and (d) the compressible flow solvers. The results from three-dimensional models and two-dimensional models are shown in black and blue, respectively. The signal arrival time  $t_{ar}$  and first crest arrival time  $t_p$  are shown by vertical gray lines for incompressible (dashed) and compressible (dotted) solvers.

$$I_1^n = \int_{-h}^0 \tilde{f}_n^2(z) = \left( \frac{1}{4\tilde{\beta}_n} \right) \left( \frac{(1-\Delta^2)2\tilde{\beta}_n h + (1+\Delta^2)\sinh 2\tilde{\beta}_n h - 4\Delta \sinh^2 \tilde{\beta}_n h}{[\cosh \tilde{\beta}_n h - \Delta \sinh \tilde{\beta}_n h]^2} \right) \quad (20)$$

$$I_2^n = \int_{-h}^0 \tilde{f}_{n,z}^2(z) = \left( \frac{\tilde{\beta}_n}{4} \right) \left( \frac{-(1-\Delta^2)2\tilde{\beta}_n h + (1+\Delta^2)\sinh 2\tilde{\beta}_n h - 4\Delta \sinh^2 \tilde{\beta}_n h}{[\cosh \tilde{\beta}_n h - \Delta \sinh \tilde{\beta}_n h]^2} \right) \quad (21)$$

$$\tilde{f}(-h) = \frac{1}{\cosh \tilde{\beta}_n h - \Delta \sinh \tilde{\beta}_n h} \quad (22)$$

where  $\Delta = \gamma/2\tilde{\beta}_n$ .

Equation (19) is the final form of the modified hyperbolic mild-slope equation for weakly compressible fluid.

#### 4. Sample Computation

Sample computations have been carried out to verify whether the mild-slope equation model (19) can be safely applied in place of a more computationally expensive 3-D treatment based on (3). In this paper, we mainly concentrate on the surface gravity wave mode to improve the arrival time of tsunami waves.

Comparison is made with MSE for weakly compressible flow with those obtained from 3-D compressible, 3-D incompressible and 2-D incompressible flow solvers. For incompressible flow,  $c \rightarrow \infty$ , the governing equation (3) reduces to Laplace's equation for the potential  $\Phi$ . We present results for two different domains consisting of vertical sections in  $(x, z)$  through laterally uniform domains with no  $y$ -dependence, therefore

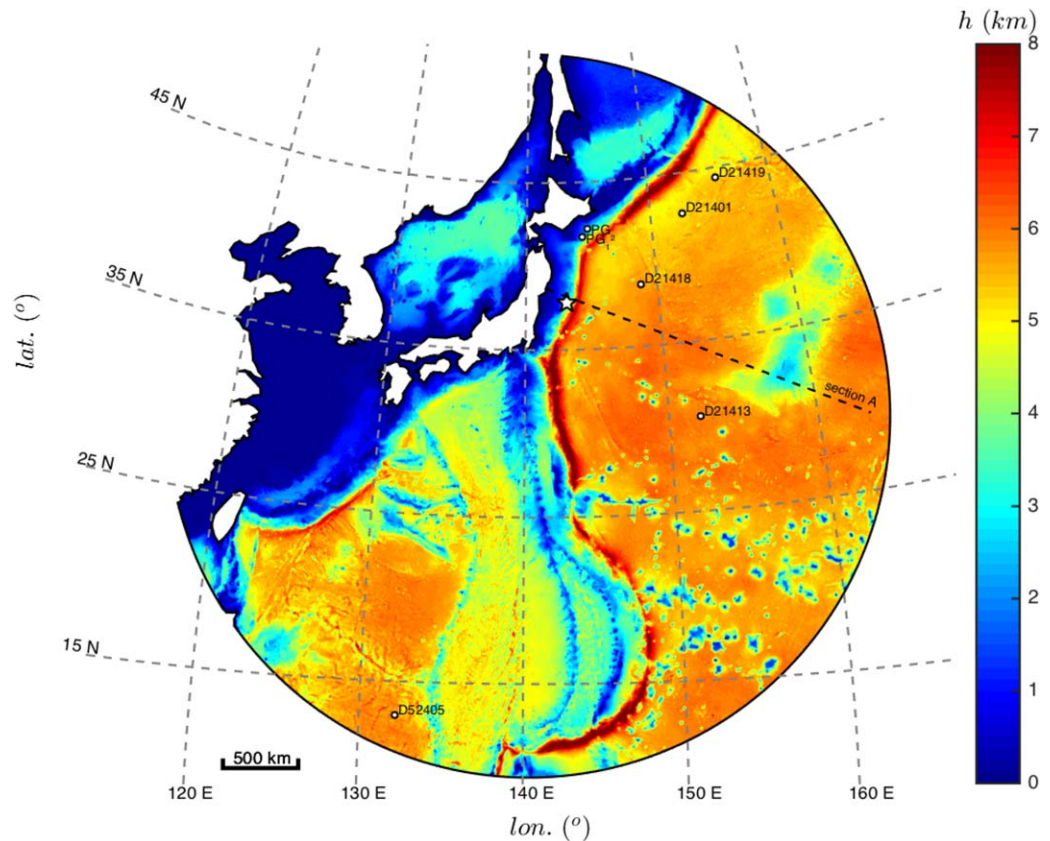


**Figure 7.** Bathymetry data (ETOPO1 and JODC data) with the position of JAMSTEC and DART bottom pressure gauges. The epicenter of 2011 Tohoku-oki event is shown by the star. The black line delimits, together with the coastline, the domain of the numerical computations. Section A is shown by dashed black line.

**Table 1**  
Coordinates of JAMSTEC and DART Sensors

Station	Latitude (°)	Longitude (°)	Depth (m)	Distance from epicenter (km)
PG <sub>1</sub>	41°42'14"N	144°26'15"E	2,200	450
PG <sub>2</sub>	42°14'11"N	144°50'54"E	2,200	515
DART#21418	38°41'17"N	148°46'09"E	5,662	510
DART#21401	42°37'00"N	152°35'00"E	5,264	970
DART#21413	30°33'14"N	152°07'50"E	5,848	1,170
DART#21419	44°22'38"N	155°41'33"E	5,320	1,300
DART#52405	12°59'07"N	132°11'01"E	5,895	2,960

the 3-D solution can be solved for 2-D domain. Similarly, the MSE can be solved along 1-D domain. The computations are done first with constant water depth and the second with varying water depth. Figure 4 shows the optimized value for  $\Delta f$  in order to reproduce 3-D wave field properly. The RMSE has been calculated for consecutive maxima in wave train between 3-D and 2-D models. Therefore, frequency bands of width  $\Delta f = 0.001$  Hz have been selected to discretize the forcing spectrum for the 0th mode covering  $0 \leq f \leq \sqrt{g/h}$ .

For the first case, the numerical solvers are applied on a computational domain 1,200 km long with constant depth  $h = 4$  km; At  $x = 0$ , monochromatic waves with three wavelengths,  $\lambda/h \sim 500, 100$ , and  $50$ , are imposed, together with a radiation to allow reflected waves to leave the domain. The wave frequencies are in the range of tsunamigenic gravitational waves, presented in Figure 2. The Sommerfeld radiation condition is applied at the open end of the domain, so that the waves leave the domain freely. To correctly

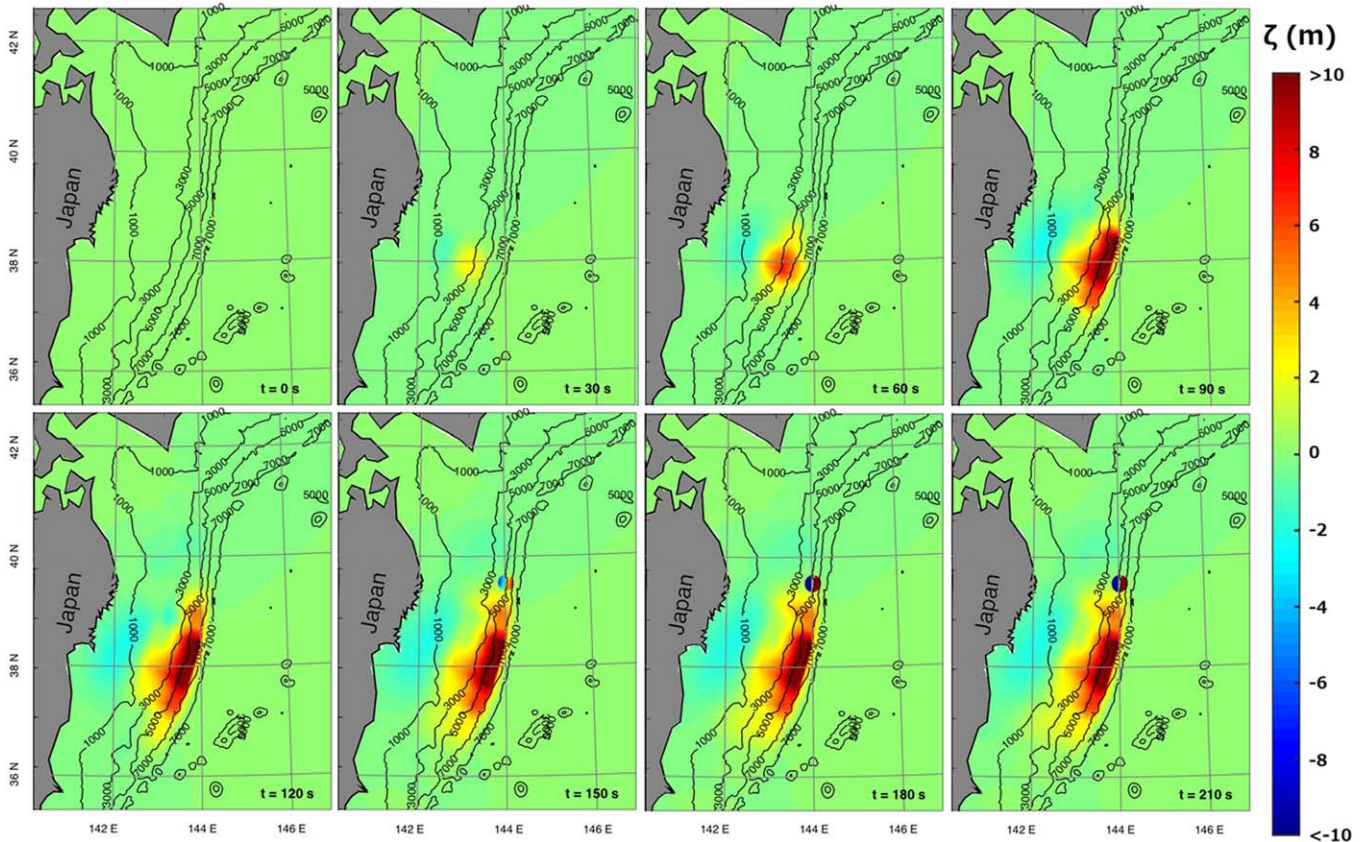


**Figure 8.** Time frames of seafloor deformation (color scale in meter) caused by the 2011 Tohoku earthquake (Grilli et al., 2013) and a dual SMF source to the north (Tappin et al., 2014) at 30 s intervals. Depth range is shown by contour lines at 2,000 m intervals.

reproduce the wave-field, the maximum mesh size is 1,000 m, for a total of 1,200 elements in the case of the depth-integrated model (equation (19)) and more than 50,000 elements for the 3-D models (equation (3)). The time step is  $dt = 5$  s and the computational time to reproduce 1,000 s of real-time simulation was approximately 5 min for (equation (19)) and approximately 1 h for 3-D solvers. A computer equipped with an i7 3.2 GHz CPU and 16 GB RAM has been used for the simulation.

A comparison of free-surface elevations at  $x = 1,000$  km between 3-D (equation (3)) and 2-D (equation (19)) models are presented for the case of compressible ocean in Figure 5. In each subplot, the 3-D and 2-D solutions are shown by solid and dashed lines, respectively. The signal arrival time,  $t_{ar} = L/c_{co}$ , is shown by vertical dashed line, where  $L$  is the distance from the monochromatic wave generator and phase celerity,  $c_{co}$ , is calculated from the solution of dispersion relation equation (11) for a given frequency and depth. The phase celerity are close to the ones calculated for the case of shallow water limit ( $kh \ll 1$ ) presented in equation (14). The 3-D model and depth-integrated model are in good agreement in prediction of the wave modulation and arrival time.

In the second case, a varying sea water depth along a vertical cross section is considered. The domain's geometry and residual bed deformation, depicted in Figure 6a, are extracted from an arbitrary line intersecting the Tohoku 2011 earthquake epicenter and deep ocean, shown in Figure 7 as section A. In Figure 6b, the approximate time lag between incompressible and compressible model is shown. At a given water depth, the phase speeds are calculated from equation (14) and subsequently travel times and time lags are evaluated. Since the reduction rate has larger values at deeper waters, at large distances and at deeper parts, the time lags accumulate, i.e.,  $\Delta t = 48$  s at a point 2,000 km from the source. The summation of the results calculated for each narrow bands of the frequency spectrum in 2-D model leads to reconstruction of 3-D results. The comparison between incompressible and compressible flow solvers and the validation of depth-integrated models are shown in Figures 6c and 6d in terms of time series of free-surface elevation  $\eta$ ,

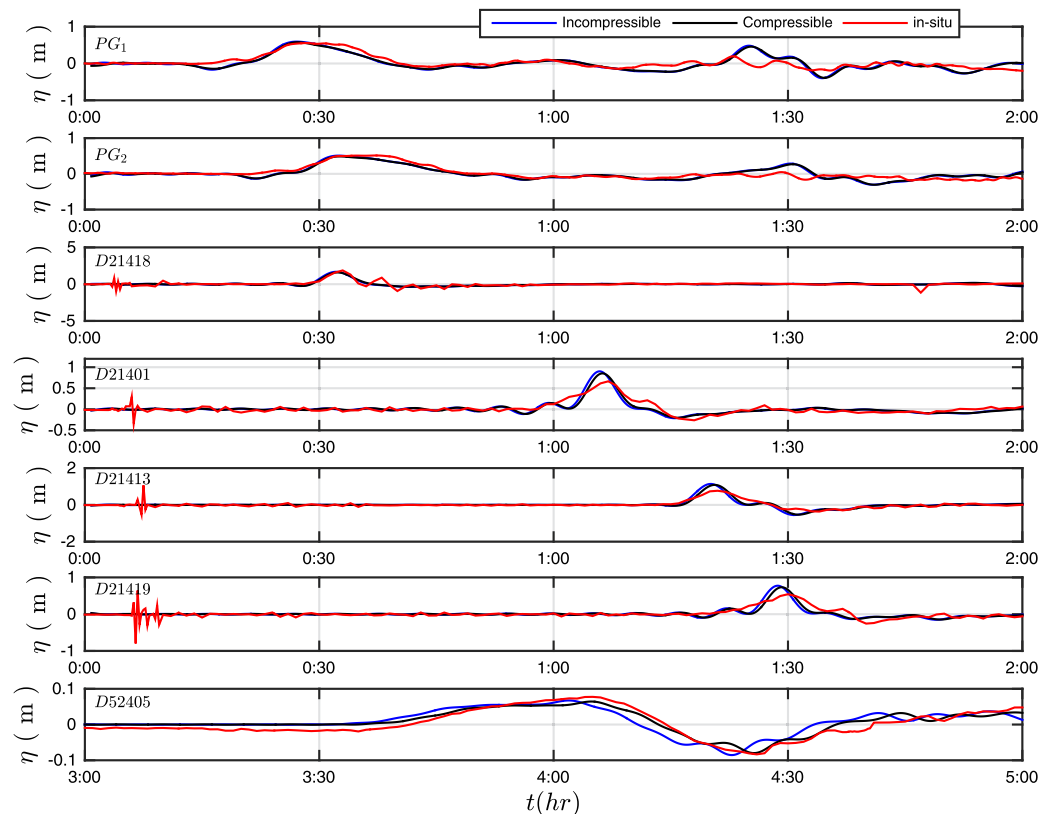


**Figure 9.** Time series of free-surface elevation ( $\eta$ ) at JAMSTEC and DART observatories  $PG_1$ ;  $PG_2$ ; DART#21418; DART#21401; DART#21413; DART#21419; and DART#52405: measured (red lines); calculated by the compressible solver (black lines) and an incompressible solver (blue lines).  $t = 0$  refers to the time of occurrence of the earthquake.

at a distance  $x_p = 2,000$  km from the coast. The signal arrival time  $t_{ar}$  and first crest arrival time  $t_p$  are shown by vertical gray lines for incompressible (dashed) and compressible (dotted) solvers. The maximum mesh size is again 1,000 m, for a total of 2,300 elements in the case of the depth-integrated model  $s$ , and 300,000 triangular elements for the 3-D ones. The time step and the discretization of the spectra are the same of the constant depth case. The computational time to reproduce 4 h of real-time simulation was about 10 min for the 2-D model and about 1.5 h for the 3-D model, using the same computer used for the previous simulation. Similar to the case of constant depth, the incompressible models predicts earlier arrival of signal and tsunami peak, shown by vertical dashed lines. On the other hand, the arrival time for the case of a compressible ocean, shown by vertical dotted lines in Figure 6d, is 48 s later than the incompressible ones. Results calculated using the 2-D and 3-D models are in good agreement, both in terms of peak amplitudes and signal/peak arrival times.

### 5. 2011 Tohoku-oki Event

On 11 March 2011, at 14:46 local time (JST), a megathrust earthquake of moment magnitude  $M_W=9.0$  occurred off the Tohoku district, north-eastern Japan, causing a devastating tsunami that resulted in over 15,800 fatalities as well as over 3,300 people missing and caused enormous destruction along the coast of Japan.

Bottom pressure data was collected during the event by the DART network and the Japan Agency for Marine-Earth Science and Technology (JAMSTEC) deep sea observatories (Table 1). Locations of observatories which recorded the waves generated by the 2011 earthquake are shown in Figure 6, together with bathymetric information within the footprint of the numerical domain described below. The DART network was deployed by the National Oceanic and Atmospheric Administration (NOAA), to support real-time forecasting of tsunami events (<http://nctr.pmel.noaa.gov/Dart/>). Tsunami warning was issued after recording

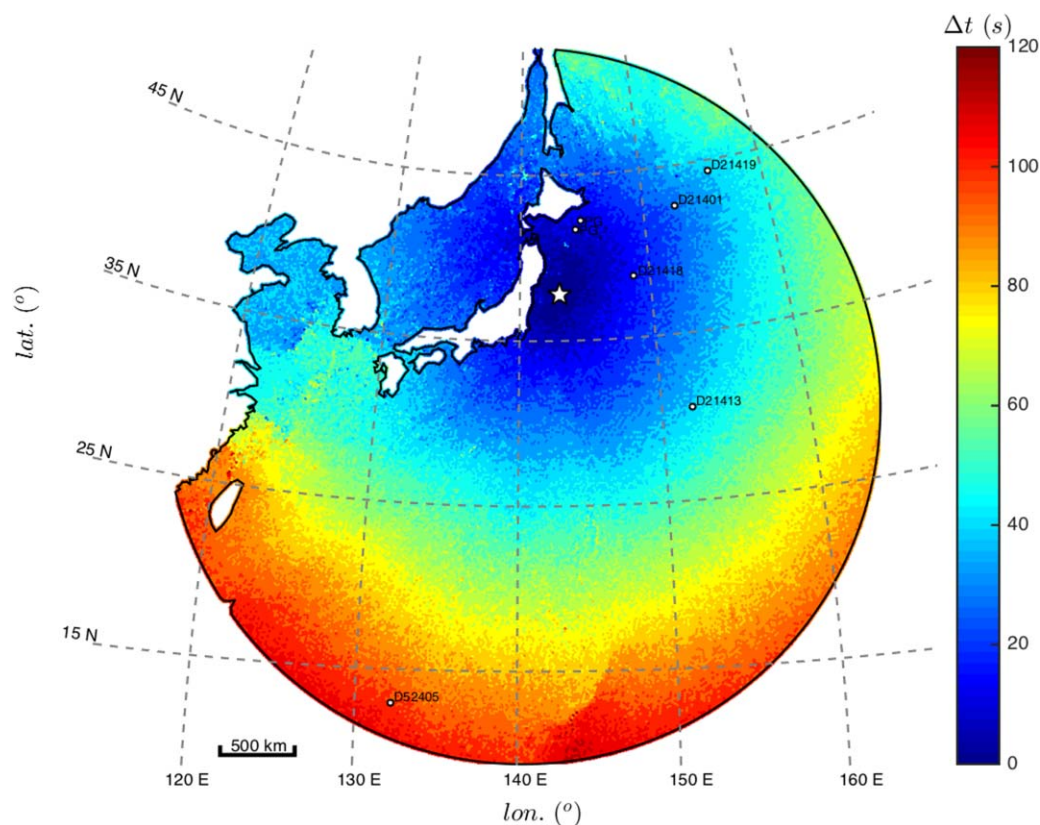


**Figure 10.** Difference between arrival time of surface gravity waves, calculated from the compressible and incompressible flow solvers.

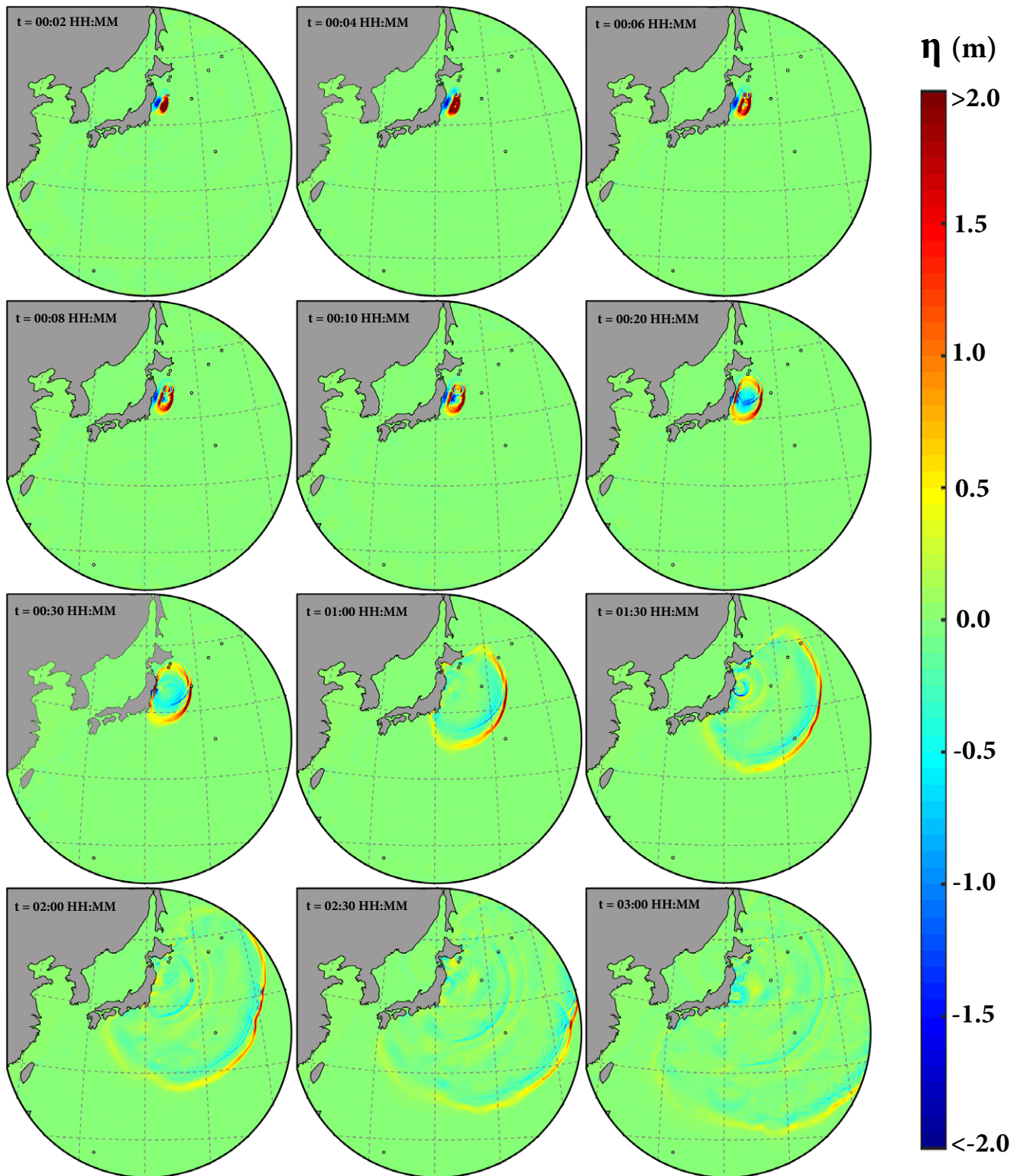


**Figure 11.** Snapshots of surface ( $\eta$ ) gravity wave elevation generated by the 2011 Tohoku-oki earthquake and SMF, computed with the hydroacoustic model.  $t = 0$  refers to the time of occurrence of the earthquake.

strong signatures of the earthquake and then of the tsunamis. The JAMSTEC cabled observatory of Hokkaido consists of three ocean-bottom seismometers (OBSs) and two ocean-bottom pressure gauges (PGs), and their data sets are sent to JAMSTEC in real time (<http://www.jamstec.go.jp/>). These observatories are equipped with many instruments, including bottom pressure recorders and seismometers (OBS1 and OBS3). The model domain and bathymetry are shown in Figure 7. The domain covers an area of about  $1.51 \times 10^7$  km<sup>2</sup>. Bathymetry data used in the numerical simulations were obtained from the National Geophysical Data Center (NGDC) database ETOPO1 (Amante & Eakins, 2009) and Japan Oceanographic Data Center (<http://www.jodc.go.jp/>).

Reconstructed seabed motion is a combination of the primary vertical displacement of the seafloor due to the earthquake (Grilli et al., 2013), and an additional tsunami source consisting of a submarine mass failure triggered after 2'15" delay and lasted for 63 s (SMF, i.e., a submarine landslide; Tappin et al., 2014). The earthquake caused mainly seabed uplift near the trench axis with a weaker subsidence nearshore with a maximum value of  $\zeta = 11.35$  m in deeper part of trench. As in Tappin et al. (2014), the SMF is a rigid slump with motion idealized as a small amplitude pendulum-like motion for the slump center of mass. The simplified SMF geometry has a quasi-Gaussian shape, similar to actual slumps. More details on the generation mechanism can be found in Tappin et al. (2014). Unlike the traditional incompressible tsunami models, which often use the residual vertical displacement of the bottom as the initial free-surface displacement, in these depth-integrated wave models, the spatiotemporal sea bottom motion is considered. The continuously varying seafloor geometry, shown by snapshots in Figure 8, is used as the boundary condition in the numerical model.

Numerical simulations of long surface gravity waves generated by the 2011 Tohoku-oki event were performed by solving for the real roots of dispersion relation, equation (11), which corresponds to the zeroth mode of equation (19). Equation (19) is solved by means of a Finite Element Method on the numerical domain of Figure 7, which has been discretized in triangular elements, here with a maximum size of 5 km. There are 2,800,000 grids for the model. The computations were done for simulation of 5 h of real time. Frequencies in the range  $f = 0-0.03$  Hz, with a  $\Delta f = 0.001$  Hz, were solved to reconstruct the gravity wave field. In a separate simulation, computation has been done using the incompressible flow solver in order to investigate the effect of ocean compressibility on tsunami wave arrival time.

Simulated free-surface elevations  $\eta$  are shown in Figure 9 at the locations of JAMSTEC observatories and at the DART buoys (Table 1). The blue and black lines show results of the incompressible and compressible numerical models, respectively, while the red lines represent the signals recorded at the instruments.

The comparison between the compressible model and the field data at the observatories shows a good agreement in terms of amplitude, period and arrival time of the signal given by the long gravity wave transit. Comparison between tsunami arrival time to the gauges from both numerical models shows that closer to the epicenter, there is no detectable difference ( $\Delta t_{PG_1} = 12$  s,  $\Delta t_{PG_2} = 13$  s, and  $\Delta t_{D21418} = 13$  s). On the other hand and for farther gauges, the compressible model predicts later arrival of tsunami waves, closer to in situ measurement ( $\Delta t_{D21401} = 27$  s,  $\Delta t_{D21419} = 40$  s,  $\Delta t_{D21413} = 40$  s, and  $\Delta t_{D52405} = 93$  s). Note that phase speed is also a function of other parameters (i.e., frequency dispersion and bottom elasticity), which are missing in present model. Also, the summation of surface gravity wave time series calculated from the compressible flow solver has better representation of signals compare to incompressible model since it divides the source frequency spectrum into discrete narrow bands with different model coefficients. As a result, each component of surface gravity wave propagate with its own phase speeds.

The time difference between the tsunami arrival time from the results of numerical simulations is shown in Figure 10. As waves propagate farther into the deeper ocean, the waves propagate faster in incompressible model. The compressible flow solver reports later arrival due to increase in reduction term  $(1 - 0.25 \times M^2)$ . Figure 11 depicts the time history of generation and propagation of tsunami waves in the computational domain. The wave front starts spreading and covers the entire domain after 3 h.

## 6. Conclusions

Inclusion of ocean compressibility in the modeling of tsunami propagation over large-scale geometries could reduce the early arrival of tsunami waves in the far distances from tsunamigenic source. In this regard,

we have therefore considered a weakly compressible inviscid fluid in which waves are generated by a moving bottom and then propagate over a mildly sloped seabed. Via a proper application of the averaging technique, we have modified the existing hyperbolic Mild Slope Equation for Weakly Compressible fluids. Solution of the equation allows the description of all the mechanics in the  $x, y$  plane, overcoming numerical difficulties. The model is first validated against three-dimensional model over vertical transects of constant and variable sea bottom. The time lag is investigated compared to incompressible flow solvers. Then, we reconstruct the gravity wave field generated by the 2011 Tohoku-oki event. Model results are compared with field data recorded during the 2011 Tohoku-oki event, by the Deep-ocean Assessment and Reporting of Tsunamis (DART) network and by the Japan Agency for Marine-Earth Science and Technology (JAMSTEC) observatories.

The mild slope model is formulated in plane Cartesian coordinates and is thus limited to medium propagation distances. Shallow water or Boussinesq models used for ocean basin scale propagation are typically formulated in spherical polar coordinates and are suitable for modeling propagation over long distances, allowing the effect of compressibility to accumulate. This work is a qualitative study on the role of ocean compressibility for generation and propagation of surface gravity waves. Although this model lacks the effect of frequency dispersion and Coriolis forces, embedded in numerical models such as Boussinesq models, as described in Kirby et al. (2013), and bottom elasticity effects (Eyov et al., 2013), it sheds lights to the role of compressibility on phase speed and draw the path toward inclusion of these effects in model equations.

#### Acknowledgments

The authors acknowledge the support of the NSF Engineering for Natural Hazards program, grant CMMI-1537232. The authors thank Stephan Grilli and Jeffrey C. Harris for providing 2011 Tohoku-oki tsunami ground motion data. The authors recognize the comments from three anonymous reviewers and thank them for these. ETOPO-1 bathymetric and topographic data used in the wave model and displayed in Figure 7 were obtained from the National Geophysical Data Center (NGDC) database (<http://maps.ngdc.noaa.gov/viewers/wcs-client/>) and Japan Oceanographic Data Center (<http://www.jodc.go.jp/>). The bottom pressure data at DART network and the Japan Agency for Marine-Earth Science and Technology (JAMSTEC) observatories are available at <http://nctr.pmel.noaa.gov/Dart/> and <http://www.jamstec.go.jp/> respectively.

#### References

- Abdolali, A., Cecioni, C., Bellotti, G., & Kirby, J. T. (2015a). Hydro-acoustic and tsunami waves generated by the 2012 Haida Gwaii earthquake: Modeling and in-situ measurements. *Journal of Geophysical Research: Oceans*, *120*, 958–971. <https://doi.org/10.1002/2014JC010385>
- Abdolali, A., Kirby, J. T., & Bellotti, G. (2015b). Depth-integrated equation for hydro-acoustic waves with bottom damping. *Journal of Fluid Mechanics*, *766*(R1), <https://doi.org/10.1017/jfm.2015.37>
- Abdolali, A., Kirby, J. T., Bellotti, G., Grilli, S. T., & Harris, J. C. (2017). Hydro-acoustic wave generation during the Tohoku-oki 2011 Earthquake. In *Proceedings of the coastal structures and solutions to coastal disasters 2015: Tsunamis* (pp. 24–34). Reston, VA: American Society of Civil Engineers.
- Allgeyer, S., & Cummins, P. (2014). Numerical tsunami simulation including elastic loading and seawater density stratification. *Geophysical Research Letters*, *41*, 2368–2375. <https://doi.org/10.1002/2014GL059348>
- Amante, C., & Eakins, B. W. (2009). *ETOPO 1 1 arc-minute global relief model: Procedures, data sources and analysis* (NOAA Tech. Memo. NESDIS NGDC-24). Boulder, CO: National Geophysical Data Center.
- Baba, T., Allgeyer, S., Hossen, J., Cummins, P. R., Tsumura, H., Imai, K., . . . Kato, T. (2017). Accurate numerical simulation of the far-field tsunami caused by the 2011 Tohoku earthquake, including the effects of Boussinesq dispersion, seawater density stratification, elastic loading, and gravitational potential change. *Ocean Modelling*, *111*, 46–54. <https://doi.org/10.1016/j.ocemod.2017.01.002>
- Baba, T., Takahashi, N., Kaneda, Y., Ando, K., Matsuoka, D., & Kato, T. (2015). Parallel implementation of dispersive wave modeling with a nesting algorithm for the 2011 Tohoku tsunami. *Pure and Applied Geophysics*, *172*, 3455–3472. <https://doi.org/10.1007/s00024-015-1049-2>
- Bondi, H. (1947). Waves on the surface of a compressible liquid. *Mathematical Proceedings of the Cambridge Philosophical Society*, *43*(1), 75–95. <https://doi.org/10.1017/S0305004100023215>
- Cecioni, C., Abdolali, A., Bellotti, G., & Sammarco, P. (2015). Large-scale numerical modeling of hydro-acoustic waves generated by tectonic earthquakes. *Natural Hazards and Earth System Sciences*, *15*, 627–636. <https://doi.org/10.5194/nhess-15-627-2015>
- Dalrymple, R. A., & Rogers, B. D. (2007). *A note on wave celerities on a compressible fluid*. Paper presented at the Proceedings of the 30th International Conference on Coastal Engineering (ICCE) 2006 (pp. 3–13). San Diego, CA.
- Eyov, E., Klar, A., Kadri, U., & Stiassnie, M. (2013). Progressive waves in a compressible-ocean with an elastic bottom. *Wave Motion*, *50*(5), 929–939. <https://doi.org/10.1016/j.wavemoti.2013.03.003>
- Grilli, S. T., Harris, J. C., Tajalli Bakhsh, T., Masterlark, T. L., Kyriakopoulos, C., Kirby, J. T., & Shi, F. (2013). Numerical simulation of the 2011 Tohoku tsunami based on a new transient FEM co-seismic source: Comparison to far- and near-field observations. *Pure and Applied Geophysics*, *170*, 1333–1359. <https://doi.org/10.1007/s00024-012-0528-y>
- Kadri, U. (2015). Wave motion in a heavy compressible fluid: Revisited. *European Journal of Mechanics: B/Fluids*, *49*(Part A), 50–57. <https://doi.org/10.1016/j.euromechflu.2014.07.008>
- Kadri, U., & Stiassnie, M. (2013). Generation of an acoustic-gravity wave by two gravity waves, and their subsequent mutual interaction. *Journal of Fluid Mechanics*, *735*, <https://doi.org/10.1017/jfm.2013.539>
- Kirby, J. T., Shi, F., Tehranirad, B., Harris, J. C., & Grilli, S. T. (2013). Dispersive tsunami waves in the ocean: Model equations and sensitivity to dispersion and Coriolis effects. *Ocean Modelling*, *62*, 39–55. <https://doi.org/10.1016/j.ocemod.2012.11.009>
- Levin, B. W., & Nosov, M. A. (2016). The physics of tsunami formation by sources of nonseismic origin. In *Physics of tsunamis* (pp. 263–309). Berlin, Germany: Springer.
- Løvholt, F., Pedersen, G. K., & Gislis, G. (2008). Oceanic propagation of a potential tsunami from the La Palma Island. *Journal of Geophysical Research*, *113*, C09026. <https://doi.org/10.1029/2007JC004603>
- Nosov, M. A., & Kolesov, S. V. (2007). Elastic oscillations of water column in the 2003 Tokachi-oki tsunami source: In-situ measurements and 3-D numerical modelling. *Natural Hazards and Earth System Science*, *7*(2), 243–249. <https://doi.org/10.5194/nhess-7-243-2007>
- Sammarco, P., Cecioni, C., Bellotti, G., & Abdolali, A. (2013). Depth-integrated equation for large-scale modelling of low-frequency hydroacoustic waves. *Journal of Fluid Mechanics*, *722*(R6), <https://doi.org/10.1017/jfm.2013.153>

- Stiassnie, M. (2010). Tsunamis and acoustic-gravity waves from underwater earthquakes. *Journal of Engineering Mathematics*, 67(1–2), 23–32. <https://doi.org/10.1007/s10665-009-9323-x>
- Tappin, D. R., Grilli, S. T., Harris, J. C., Geller, R. J., Masterlark, T., Kirby, J. T., . . . Mai, P. M. (2014). Did a submarine landslide contribute to the 2011 Tohoku tsunami? *Marine Geology*, 357, 344–361. <https://doi.org/10.1016/j.margeo.2014.09.043>
- Wang, D. (2015). An ocean depth-correction method for reducing model errors in tsunami travel time: Application to the 2010 Chile and 2011 Tohoku tsunamis. *Science of Tsunami Hazards*, 34(1), 1–22.
- Watada, S. (2013). Tsunami speed variations in density-stratified compressible global oceans. *Geophysical Research Letters*, 40, 4001–4006. <https://doi.org/10.1002/grl.50785>
- Watada, S., Kusumoto, S., & Satake, K. (2014). Traveltime delay and initial phase reversal of distant tsunamis couple with the self-gravitating elastic earth. *Journal of Geophysical Research: Solid Earth*, 119, 4287–4310. <https://doi.org/10.1002/2013JB010841>
- Yamazaki, Y., Cheung, K. F., & Kowalik, Z. (2011). Depth-integrated, non-hydrostatic model with grid-nesting for tsunami generation, propagation and run-up. *International Journal for Numerical Methods in Fluids*, 67, 2081–2107. <https://doi.org/10.1002/flid.2485>